minerals

MDPI

Article

Petrophysical Acoustic Characterization of Weathered Granite: A Case Study of Mesozoic Granites in the Coastal Area of Fujian Province, China

Zhiwen Tian [1], Jinshui Liu [2], Huafeng Tang [1,*], Wenrui Ma [2], Peng Tao [1], Zhe Dong [2] and Jingsong Hu [1]

1 College of Earth Sciences, Jilin University, Changchun 130061, China
2 Shanghai Branch, CNOOC China Limited, Shanghai 200030, China
* Correspondence: tanghfhc@jlu.edu.cn

Abstract: In recent years, with the exploration and development of granite buried-hill oil and gas reservoirs, petrophysics research has played an important role in the study of reservoir characteristics and fluid identification. Through analysis of the relationship between the fluid-bearing petrophysical parameters and the reservoir, the seismic response changes caused by reservoir fluid changes can be determined. Mesozoic granites in the coastal area of Fujian Province in eastern China were investigated as the research object of this project. The mineral composition, density, porosity, P-wave velocity, and S-wave velocity of the granite were measured and analyzed by X-ray diffraction, rock density, rock porosity, and rock acoustics methods. Therefore, the granite's petrophysical properties, fluid response characteristics, and gas sensitivity parameters were analyzed. The result of the study shows that the granite is predominantly monzogranite. According to the type of reservoir space assemblage, the samples can be divided into two types: those containing fracture-dissolution pores and those containing only dissolution pores. All the samples were characterized by medium to high densities and low to extra-low porosity. There was a linear correlation between the P-wave velocity and S-wave velocity under gas and water-saturated conditions. Factors such as P-wave to S-wave velocity ratio, Poisson's ratio, Lame coefficient, and other parameters of the samples were analyzed, and the threshold values that distinguished the water and gas-saturated states of the samples were measured and determined. In addition, there were negative correlations between the P- and S-wave velocities and porosity. The sensitivities of the petrophysical parameters to the gas capacity from high to low are $Ip^2 - 2.03\ Is^2$, $\lambda - 0.03\ \mu$, λ, λ/μ, $E - 2.03\ \mu$, σ, K/μ, K, Ip, Vp/Vs, Vp, E, μ, Vs, and Is. For granite-buried hill reservoirs, the variation ranges of the parameters, such as the density, porosity, and P-wave velocity, of the fracture-dissolution pore granite samples were larger than those of the dissolution pore samples. The bulk parameters (Ip, Vp, K, λ) and combination parameters ($Ip^2 - 2.03\ Is^2$, K/μ, $\lambda - 0.03\ \mu$, $E - 2.03\ \mu$, λ/μ) of the dissolution pore samples were more sensitive to the gas capacity. The results of this study provide a basis for the geophysical identification of granite-buried hill reservoirs.

Keywords: mesozoic; granites; petrophysical properties; gas sensitive parameters; buried hill reservoir

Citation: Tian, Z.; Liu, J.; Tang, H.; Ma, W.; Tao, P.; Dong, Z.; Hu, J. Petrophysical Acoustic Characterization of Weathered Granite: A Case Study of Mesozoic Granites in the Coastal Area of Fujian Province, China. *Minerals* **2023**, *13*, 514. https://doi.org/10.3390/min13040514

Academic Editor: Amin Beiranvand Pour

Received: 8 February 2023
Revised: 25 March 2023
Accepted: 4 April 2023
Published: 6 April 2023

1. Introduction

Buried hill oil and gas reservoirs are widely distributed in basins all over the world [1–3]. With the improvement of exploration theory and technology, buried hill oil and gas reservoirs have become an important study field in oil and gas exploration [4–9]. In recent years, PL9-1, BZ19-6, YL8-1, and other large oil and gas fields have been discovered in China's offshore basins [10–13]. Due to the high commercial and economic value of fossil fuels, granite-buried hill oil and gas reservoirs have attracted extensive consideration again [5,9]. For granite-buried hill reservoirs, identification of the reservoir is of great importance to reservoir research and for the selection of favorable exploration areas. Currently, several theories and techniques have been developed in the study of granite-buried hill reservoirs. For instance, weathering crust reservoirs have obvious vertical zoning (clay weathering zone, sandy gravel weathering zone, fracture zone, and bedrock zone) with different structures and textures containing different reservoir spaces (pore type, fracture-pore type, pore-fracture type, fracture type) [14–19]. The reservoir space of the weathering dissolution zone is dominated by dissolution pores. The reservoir space of the fracture zone is dominated by fractures. The research on the buried hill reservoir is mainly performed by using seismic, logging, and drilling methods. For offshore basins, core observation and well logging can be used for analysis if there is drilling; otherwise, seismic data can only be used if there is no drilling. The rock acoustic characteristics are fundamental to the basis for seismic response analysis of a reservoir's geological attributions. Different physical parameters can be obtained by rock acoustic analysis. Different petrophysical parameters respond differently to reservoirs [20]. For example, shear parameters are not sensitive to fluid but are helpful for lithology identification. The physical parameters reflect the coupling of the solid medium, its structure, and fluid. The sensitivity difference of combined parameters to reservoir fluid is more prominent higher than that of a single parameter. Therefore, the rock acoustic characteristics analysis can be helpful for the study of the granite-buried hill reservoir. However, there are few studies on the acoustic characteristics of granite-buried hill reservoirs [20–22].

The granite-buried hill in the East China Sea basin has certain exploration prospects. Unfortunately, due to the difficulty of obtaining granite samples from buried hills in the East China Sea basin, relevant studies have not been carried out [23]. To clarify the physical acoustic characteristics of the granite buried hill, the present study investigated the petrological, reservoir, and acoustic parameters of the weathered granite field on terrene around the East China Sea basin. Specifically, the relationships between the reservoir and the petrophysical parameters were assessed, and the fluid-sensitive parameters were identified. In addition, the better influence of different reservoir spaces on the petrophysical and fluid-sensitive parameters was discussed. The results of this study lay a foundation for seismic identification and fluid identification of granite-buried hill reservoirs in marine basins.

2. Geologic Setting

In eastern China, the paleo-Pacific Plate continued to converge towards Eurasia during the Mesozoic, resulting in the development of abundant intermediate-felsic intrusive rocks in the southeastern coast of China, Hainan Island, southern Vietnam, and southwestern Borneo [24–29]. Furthermore, Indosinian, Early Yanshanian, and Late Yanshanian granites developed in the southeastern coastal areas of China (Figure 1a). The age of the granite in our study area is Late Yanshanian (120–85 Ma) which formed under the background of the forward subduction tectonic system of the Pacific Plate [26].

According to the apatite fission track data, the granites in the study area experienced rapid cooling and uplift processes and were exposed to the surface during the Late Cretaceous. From the Late Cretaceous to the present, they have experienced slow cooling and uplift [30,31]. The granite in the study area has also undergone weathering and erosion for a long time, which is similar to the Late Cretaceous–Paleocene granite buried hills in the East China Sea basin [23]. However, the difference between these granites is that the granites buried in the sea basin formed buried hills after the Paleocene. In terms of their petrogenesis, mineral composition, temperature reduction and uplift processes, and regional tectonic setting, the granite weathering crust reservoirs in the marine basin and terrene areas are comparable. Therefore, the weathered granite in the land area around the basin can provide a reference for the granite in the buried hill in the basin. To better understand the properties of granite from this area, samples were collected from the coastal areas of Fujian Province. The sampling locations are shown in Figure 1b.

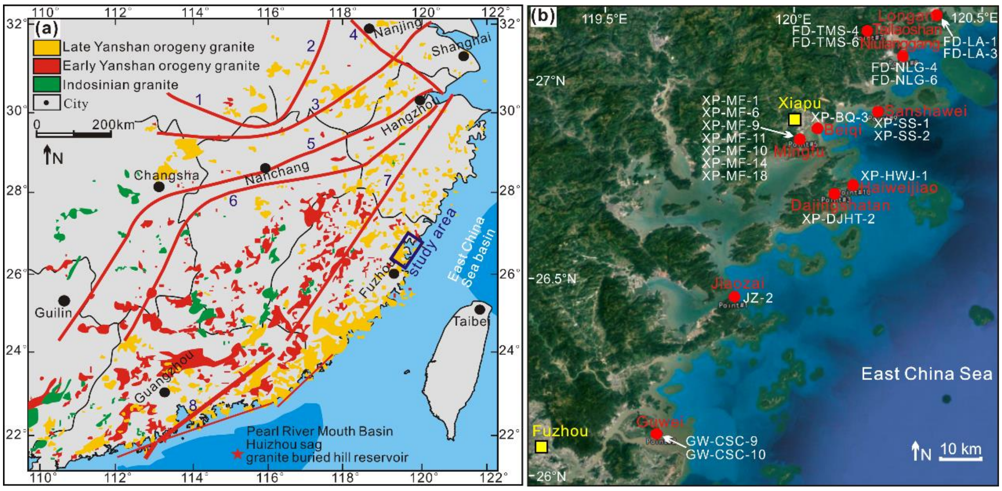

Figure 1. Location of the study area. (**a**) Distribution characteristics of granite in southeastern coastal area (after Mao et al. (2014) [26]). (**b**) sample locations. 1. Southern Dabie Mountain fault; 2. Tancheng-Lujiang fault; 3. Nantong-South Liyan-South Lushan-Ruichang-Chongyang fault; 4. Chuzhou-Jiaxing fault; 5. Hangzhou-Xiangtan-Jinxiu-Pingxiang fault; 6. Shaoxing-Jiangshan-Pingxiang-Wuzhou-Hepu fault; 7. Yuyao-Zhenghe-Dapu fault; 8. Lianhuashan fault.

3. Analytical Methods

Numerous granite samples were collected from the Xiapu and Lianjian counties and analyzed.

3.1. X-ray Diffraction

A total of 21 granite samples were analyzed. The testing unit was the Key Laboratory of Mineral Resources Evaluation of Northeast Asia, Ministry of Natural Resources, Jilin University. The experiment steps are as follows. First, remove the weathered surface from the samples and take 15 g of fresh samples. Wash the sample surface with distilled water and dry it (60 °C, 24 h). Secondly, the sample was pulverized to 200 mesh using the GJ-1 crusher to make the sample completely mixed. The X-ray diffraction instrument was a DX-2700 X-ray diffractometer, rated power 4 KW, with angle accuracy less than 0.005°, angle setting speed 120°/min, and energy spectrum resolution less than 25% with Cu K-alpha radiation. Finally, according to the diffraction curve, 2θ value, relative intensity, and diffraction peak width, the mineral composition and content were analyzed on the computer using MDI Jade software. The details of processing and related parameters are described by Xu et al. (2015) [32].

3.2. Density

The densities of the samples were measured at the Institute of Acoustics of the Chinese Academy of Sciences. The samples were cut into a cylinder with a diameter of 25 mm and a length of 50 mm, which were washed with distilled water, dried at 60 °C for 24 h, and naturally cooled for later use. The exact diameter and length of the cylindrical sample were measured using Vernier calipers, and the volume of the rock samples was calculated using the measured geometric dimensions. Next, an electronic balance was used to measure the weight (W) of the dry rock sample. Finally, the dry density of the rock sample was calculated as the weight divided by the volume. In total, the densities of 21 samples were obtained. The details of processing and related parameters are described by Chen et al. (2010) [21].

3.3. Porosity

The Porosities of the samples were analyzed at the Institute of Acoustics of the Chinese Academy of Sciences. The rock samples were completely saturated with pure water under a vacuum. The saturation weight W1 was determined using an electronic balance. Then, the weight of the water in the sample W2 was subtracted from the dry sample weight W, i.e., W2 = W−W1. Next, W2 was divided by the density of pure water to obtain the pore volume V1. Finally, the porosity of the rock sample was obtained by dividing V1 by the dry rock sample volume V. The porosity of 21 samples was obtained. The vacuum pumping pressure saturation method was used to saturate the rock samples in water using a BH-1 core vacuum pressurized saturation device. The saturation pressure was set to 9 MPa, the saturation time was 48 h, the saturated medium was pure water, and the ambient temperature was 20 °C. The details of processing and related parameters are described by Li et al. (2012) [33].

3.4. Acoustic Parameter P-Wave and S-Wave Analysis

The acoustic parameter P-wave and S-wave analysis was conducted at the Institute of Acoustics of the Chinese Academy of Sciences and was conducted using the transmission method. The Olympus B2 couplant was applied evenly between the sample and the sonic probe end cap to ensure adequate coupling between the sample and the sonic probe end cap. The Olympus B2 couplant is used to reduce the tiny pores between the acoustic probe and sample and reduce the influence of microair on ultrasonic. Next, the sample was fixed on the test stand for ultrasonic testing. The P-wave and S-wave data for the saturated samples were collected and recorded using a computer. The data were analyzed to determine the arrival time and velocity of the sample wave by determining the sample length and arrival time of the first wave using an Agilent MS07034B oscilloscope, an Olympus 5077PR ultrasonic pulse generator, and an Olympus 1 MHz acoustic probe. The ultrasonic measurement transducer frequency is 0.1 MHz. The dynamic elastic parameters of rock are calculated by the velocity and time difference of P- and S-wave. The dynamic parameters of rock are mainly elastic Young's modulus (E), bulk modulus (K), shear modulus (μ), Poisson's ratio (σ), Lame coefficient (λ), P-wave impedance (Ip), and S-wave impedance (Is). See Appendix A for the calculation method and data. The details of processing and related parameters are described by Chen et al. (2010) [21].

4. Dataset and Results

4.1. Rock Minerals and Reservoir Space Composition

Petrographic microscope studies show that the rocks were observed to have either allotriomorphic or hypautomorphic granular texture. The phenocrysts are quartz, plagioclase, and alkaline feldspar, and the dark minerals are mainly biotite (1%–5%). Through the identification of 21 samples, we were able to determine that the lithology of the samples is mainly monzogranite (Figure 2a–c), with a small amount of granodiorite and quartz monzonite (Figure 2d). These results were confirmed using X-ray diffraction, which yielded a quartz content of 17%–46%, an alkaline feldspar content of 18%–47%, and a plagioclase content of 20%–55%. Plagioclase to alkaline feldspar ration is 38%–75%. Based on the Quartz–Alkali feldspar–Plagioclase (QAP) diagram, one sample plot was in the quartz monzonite region, three samples plot were in the granodiorite region, and the rest of the samples plot was in the monzonite region (Figure 3).

Overall, the samples are dense and massive, with a few fractures and dissolution pores. The fractures observed in the outcrop were shear fractures and weathering fractures. Due to the limitations of the sample preparation, there are only weathering fractures in the sample, which penetrated the mineral grains and had widths that measured between 5–15 μm. Furthermore, two types of fractures were observed under the microscope: (1) fractures that were irregular in shape and highly filled (Figure 2b) and (2) fractures that had a regular plane and a low degree of filling (Figure 2c). Dissolution pores are widely distributed and are mainly intergranular micropores produced during biotite chloritization (Figure 2b–d), alkaline feldspar and plagioclase montmorillization, and kaolinization. According to the composition of the reservoir spaces, the samples were divided into two types: samples with both fracture and dissolution pores (9 samples) and samples with only dissolution pores (12 samples) (Table 1).

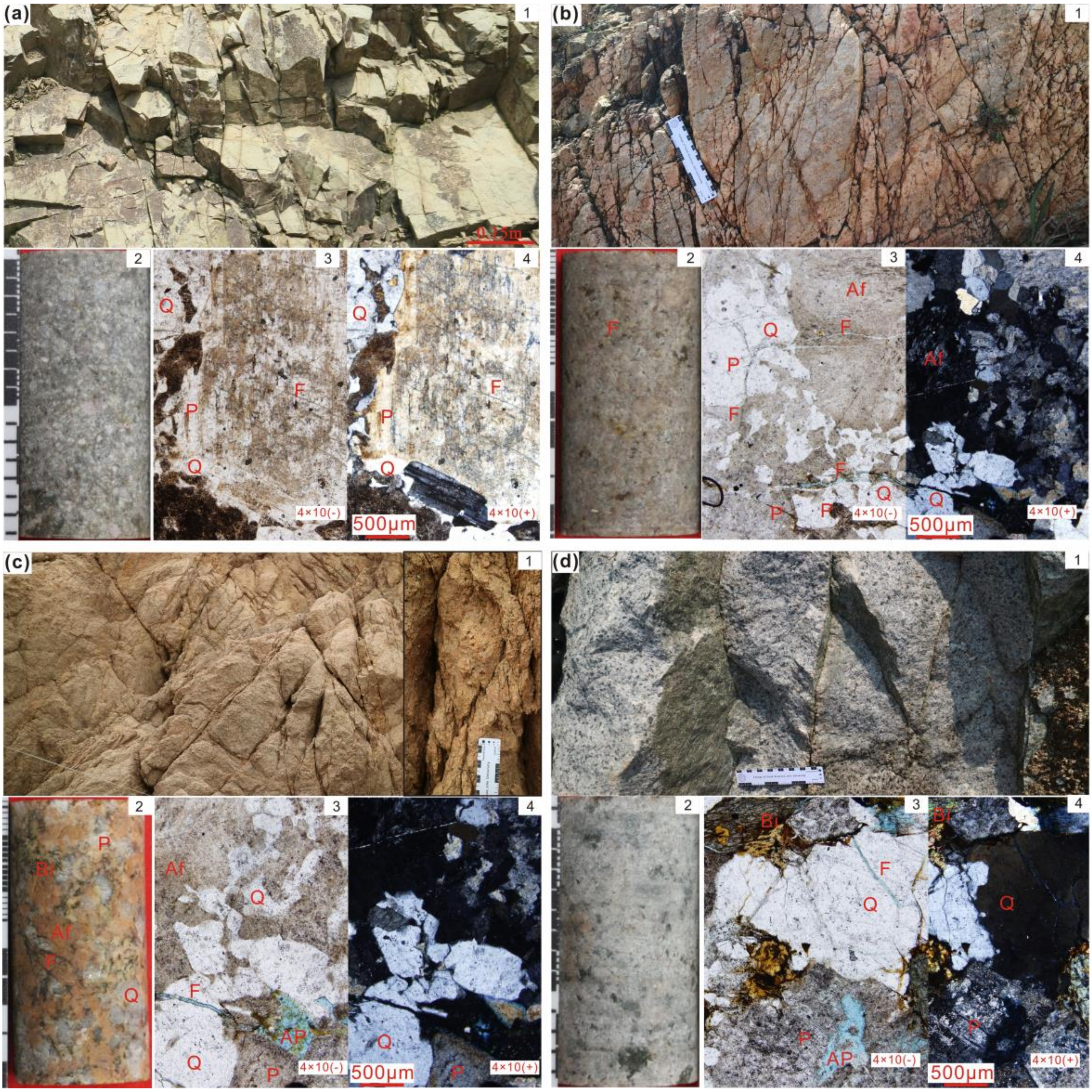

Figure 2. Mineral and fracture characteristics of Mesozoic granite samples from the coastal area of Fujian Province. (**a**) FD-LA-3 monzogranite; (**b**) FD-NLG-6 monzogranite; (**c**) FD-TMS-6 monzogranite; (**d**) XP-MF-11, granodiorite. Af-alkali feldspar; AP-dissolution pore; Bi-biotite; Chl-chlorite; F-fracture; P-plagioclase; Q-quartz. 1-field photograph, 2-sample picture, 3-single polarizing microscope photograph, 4-orthogonal polarized microscope photograph. The microscope type is OLYMPUS BX51.

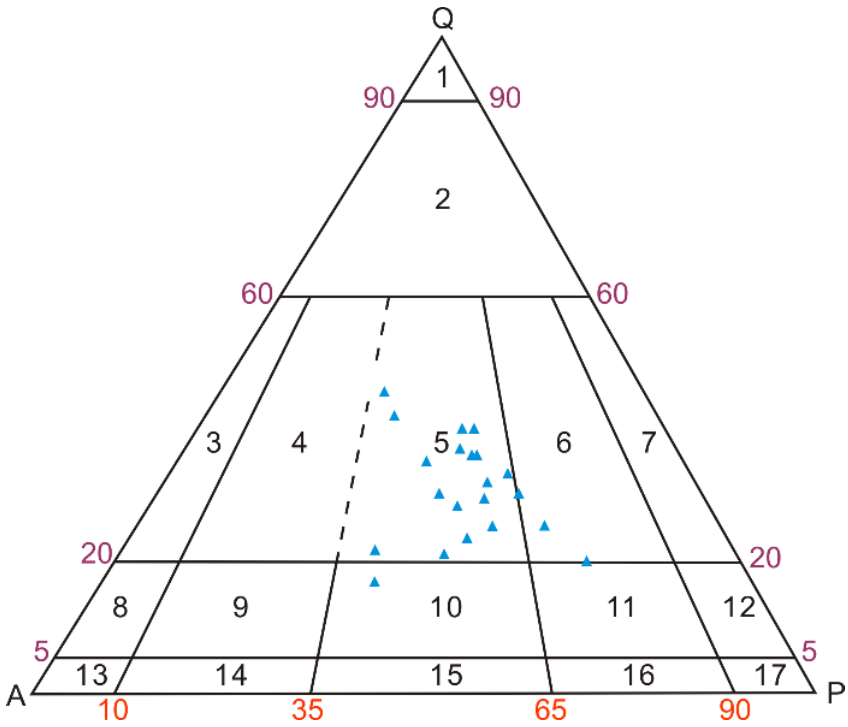

Figure 3. QAP diagram of the Mesozoic intrusive rocks in the coastal area of Fujian Province. 1-quartzolite; 2-quartz-rich granite; 3-alkali-feldspathic granite; 4-syenogranite; 5-monzogranite; 6-granodiorite; 7-tonalite; 8-quartz-alkali feldspar; 9-quartz syenite; 10-quartz monzonite; 11-quartz monzodiorite/quartz monzonite gabbro; 12-quartz diorite/quartz gabbro/quartz anorthosite; 13-alkali feldspar syenite; 14-syenite; 15-monzonite; 16-monzodiorite/monzogabbro; 17-diorite/gabbro/anorthosite.

4.2. Density and Porosity Characteristics

The density and porosity of the samples are shown in Figure 4. The granite samples have medium-high densities that range from 2.2–2.7 g/cm^3, mostly between 2.4–2.7 g/cm^3, with a geometric mean of 2.52 g/cm^3. The density and porosity test results for the granite samples indicate that the reservoir has a low to extra-low porosity that ranges from 0.99% to 10.00%, with a geometric mean of 3.87%.

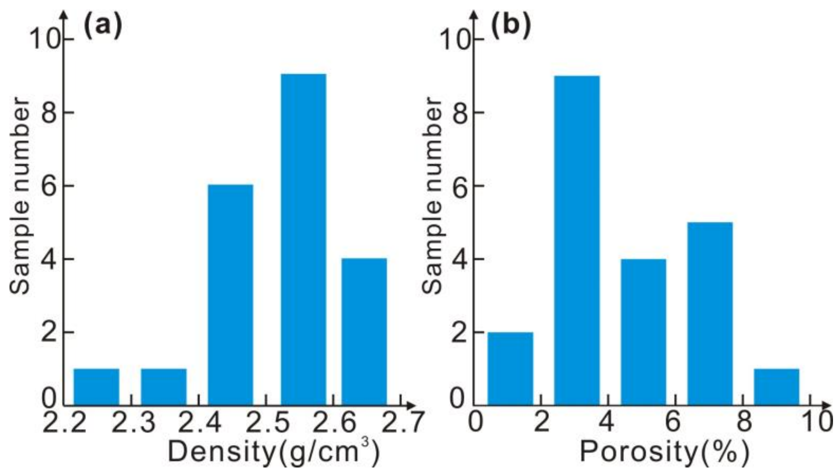

Figure 4. Density (**a**) and porosity (**b**) histograms of the Mesozoic granites in the coastal area of Fujian Province.

Table 1. X-ray diffraction analysis results and reservoir space types for Mesozoic granite samples from the coastal area of Fujian Province.

Location	Sample Number	Lithology	Quartz (%)	K-Feldspar (%)	Plagioclase (%)	Biotite (%)	Muscovite (%)	Amphibole (%)	Chlorite (%)	Calcite (%)	Reservoir Space
Jiaozai, Lianjiang County	JZ-2	quartz monzonite	17	47	33	3	–	–	–	–	AP
Guwei Quarry, Lianjiang County	GW-CSC-9	monzogranite	25	29	44	2	–	–	–	–	F-AP
	GW-CSC-10	granodiorite	30	23	44	2	1	–	–	–	AP
Mingfu quarry, Xiapu County	XP-MF-1	monzogranite	29	29	41	1	–	–	–	–	AP
	XP-MF-6	monzogranite	22	44	31	2	–	1	–	–	AP
	XP-MF-9	monzogranite	28	29	34	4	–	5	–	–	F-AP
	XP-MF-10	monzogranite	21	32	35	4	–	6	2	–	F-AP
	XP-MF-11	granodiorite	25	20	45	4	1	–	5	–	AP
	XP-MF-14	granodiorite	20	18	55	4	–	–	3	–	F-AP
	XP-MF-18	monzogranite	32	25	38	2	–	–	3	–	F-AP
Haiweijiao, Xiapu County	XP-HWJ-1	monzogranite	33	23	41	3	-	–	–	–	AP
Sansha Xiapu County	XP-SS-1	monzogranite	36	26	36	1	–	–	–	1	AP
	XP-SS-2	monzogranite	40	26	33	1	–	–	–	–	AP
Beiqi, Xiapu County	XP-BQ-3	monzogranite	42	32	24	2	–	-	–	–	F-AP
Longan quarry, Fuding County	FD-LA-1	monzogranite	37	26	32	2	3	–	–	–	AP
	FD-LA-3	monzogranite	40	24	33	2	1	–	–	–	AP
Niulanggang, Fuding County	FD-NLG-4	monzogranite	46	32	20	1	1	–	–	–	F-AP
	FD-NLG-6	monzogranite	30	33	35	2	–	–	–	–	F-AP
Tailaoshan, Fuding County	FD-TMS-4	monzogranite	36	27	36	1	–	–	–	–	AP
	FD-TMS-6	monzogranite	35	33	30	2	–	–	–	–	F-AP
Dajing, Xiapu County	XP-DJHT-2	monzogranite	23	32	40	5	–	–	–	–	AP

Note: F-AP denotes fractures and dissolution pores; AP denotes dissolution pores.

4.3. P-Wave and S-Wave Velocities of Granite

For the granite samples in the gas-saturated condition, the P- and S-wave velocities were 2841–5507 m/s (with a geometric mean of 4111 m/s) and 1646–3623 m/s (with a geometric mean of 2683 m/s), respectively. In the water-saturated condition, the P- and S-wave velocities were 3634–5890 m/s (with a geometric mean of 4664 m/s) and 1646–3859 m/s (with a geometric mean of 2640 m/s), respectively. Figure 5 shows that there is a good linear correlation between the P-wave and S-wave velocities of the granite samples under the gas and water-saturated conditions. Since the P-wave velocity of the water-saturated sample increases obviously while the s-wave velocity hardly changes, the fitting line of the saturated sample is located below the gas-filled sample. Because the P-wave velocity increases obviously, there is almost no change in the S-wave velocity after the sample is saturated with water; the fitting line of the water-saturated sample is located below the gas-saturated sample. Data see Appendix A.

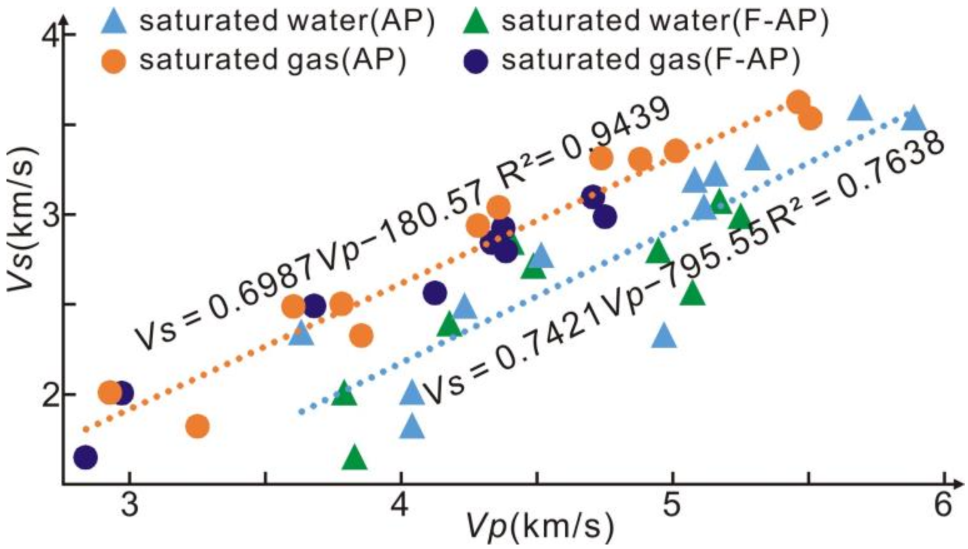

Figure 5. Cross plot of P-wave and S-wave velocities of the Mesozoic granites in the coastal area of Fujian Province. F-AP denotes fractures and dissolution pores samples. AP denotes dissolution pores samples.

5. Petrophysical Responses of Pores and Fluids

5.1. Relationships between P-Wave and S-Wave Velocities and Porosity

Reservoir porosity is a key parameter for exploration target evaluation and reserve estimation. Figure 6 shows the variations in the P-wave velocity and S-wave velocity with porosity under different fluid saturation conditions. The critical value of the correlation coefficient was determined to be 0.433 when the degree of freedom equaled 19, with a significance level of $\alpha = 0.05$. The correlation coefficients (R) between the P-wave and S-wave velocity and porosity are negative, but the absolute values are greater than the critical values (Table 2). Therefore, the wave velocities are negatively correlated with the porosity. The P-wave and S-waves velocities decrease with increasing porosity, and the correlation between the P-wave velocity and porosity for the water-saturated samples was the best. Figure 6c shows that for a given porosity, the P-wave velocity of the water-saturated sample is larger than that of the gas-saturated sample. Figure 6d shows that the fitting lines of the S-wave velocity in the two states are close (theoretically, the S-wave velocity does not change under fluid-saturated conditions). For a given porosity, the S-wave velocities of the water-saturated and gas-saturated samples are very similar.

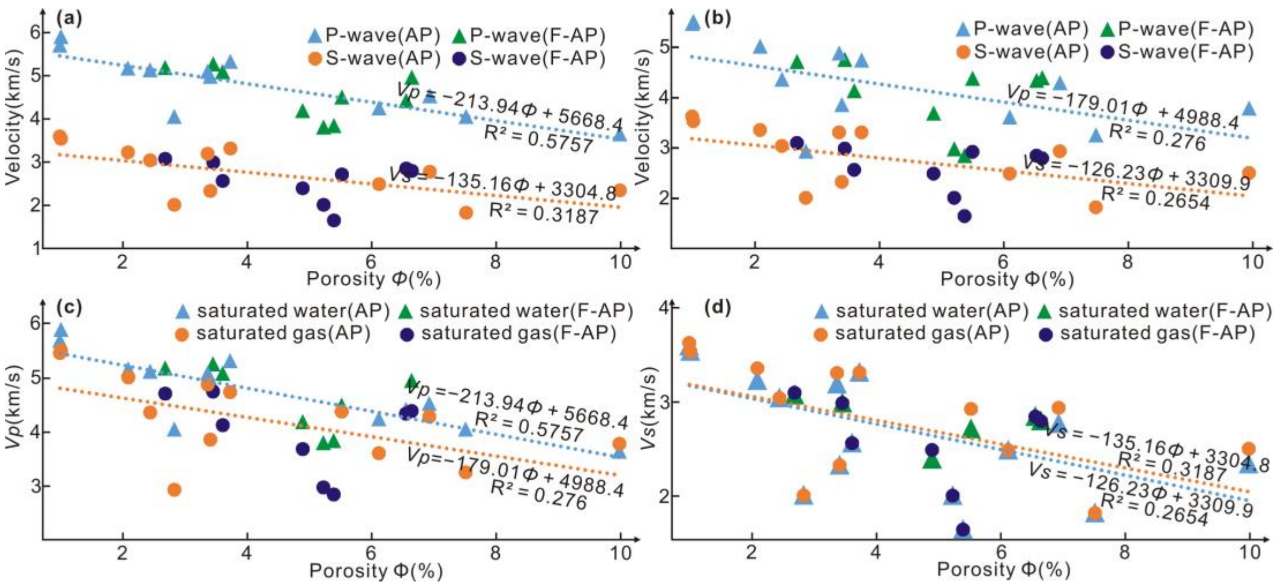

Figure 6. Cross plot of velocity and porosity of the Mesozoic granites in the coastal area of Fujian Province under gas-saturated and water-saturated conditions. (**a**) Relationship between velocity and porosity under water-saturated conditions; (**b**) relationship between velocity and porosity under gas-saturation conditions; (**c**) relationship between P-wave velocity and porosity; (**d**) relationship between S-wave velocity and porosity. F-AP denotes fractures and dissolution pores samples. AP denotes dissolution pores samples.

Table 2. Comparison of related characteristics of acoustic velocity and porosity.

Acoustic Velocity	Fitting Function	Relevance (R^2)	Correlation Coefficient	Freedom/n − 2	Correlation Critical Value (R)
Saturated water P-wave	$Vp_{\mathrm{w}} = -213.94\Phi + 5668.4$	0.5757	−0.76	19	0.433
Saturated water S-wave	$Vs_{\mathrm{w}} = -135.16\Phi + 3304.8$	0.3187	−0.56	19	0.433
Saturated gas P-wave	$Vp_{\mathrm{g}} = -179.01\Phi + 4988.4$	0.276	−0.53	19	0.433
Saturated gas S-wave	$Vs_{\mathrm{g}} = -126.23\Phi + 3309.9$	0.2654	−0.52	19	0.433

5.2. Petrophysical Response of Fluids

In this study, the changes in the petrophysical characteristics under water and gas-saturated conditions were analyzed. From the perspective of single parameters, such as the P-wave to S-wave velocity ratio, the Poisson's ratio, and the Lame coefficient, it can distinguish between the water and gas-saturated states. The ratio of P- and S-wave can be used to distinguish between water and gas-containing samples (Figure 5). Taking 1.6 as the threshold value, ratios greater than 1.6 indicate that the sample contains water, and ratios less than 1.6 indicate that the sample contains gas. Using this criterion, five samples were misidentified, and six samples were located near the threshold value (Figure 7a). For a Poisson's ratio threshold of 0.18, values less than 0.18 indicate that the sample contains gas. However, four samples containing gas were incorrectly classified as containing water, and two samples containing water were incorrectly classified as containing gas (Figure 7b). For a Lame coefficient threshold value of 12.5 GPa, a value of less than 12.5 GPa indicates that the sample contains gas. One sample containing gas was incorrectly classified as containing water, and two samples containing water were incorrectly classified as containing gas (Figure 7c). Of the three coefficients, the Lame coefficient was the most accurate in determining the gas and water content of the samples.

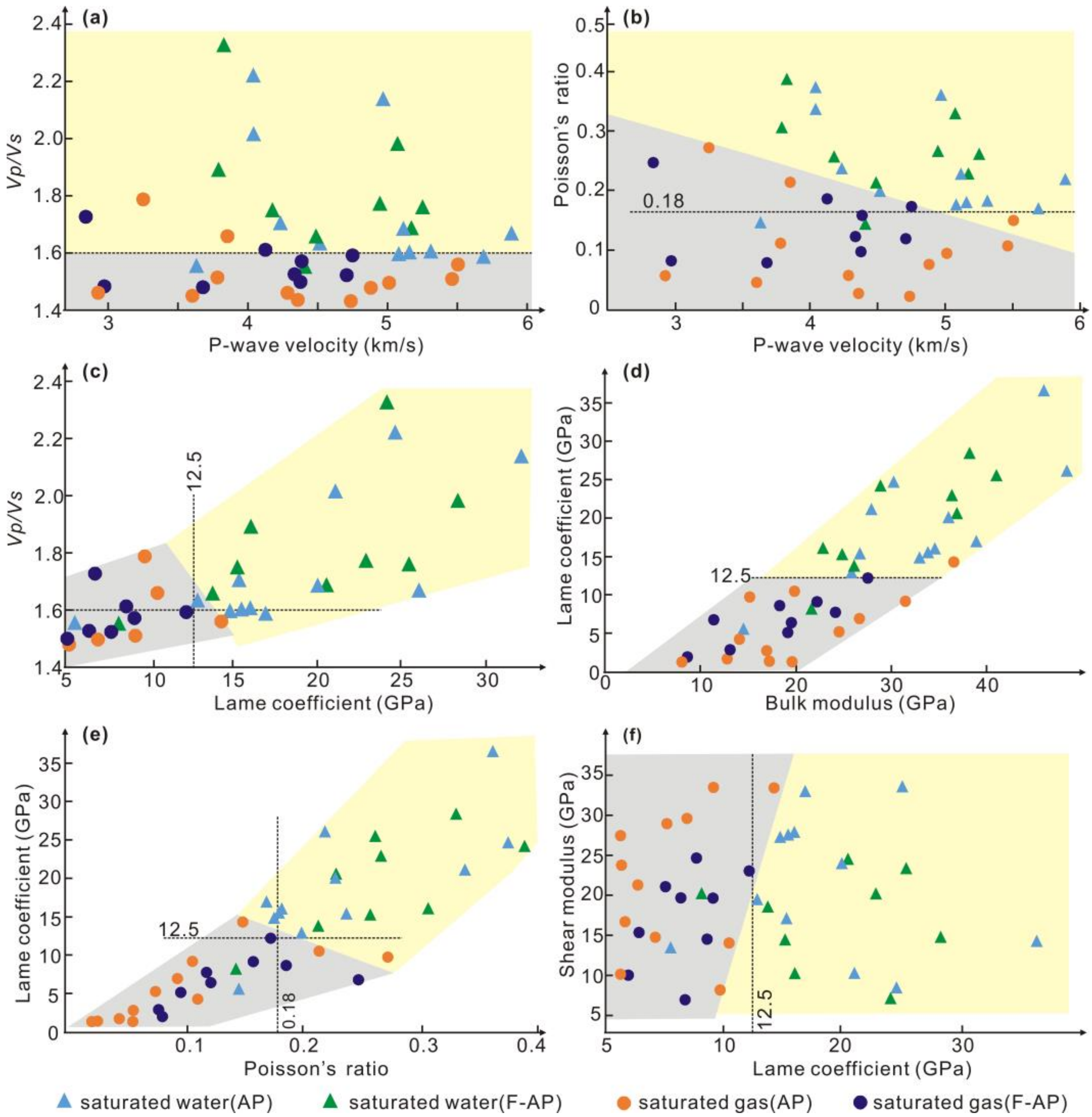

Figure 7. Petrophysical response of Mesozoic granites in the coastal area of Fujian Province to fluids. (**a**) relationship between *Vp* and *Vp*/*Vs*; (**b**) relationship between *Vp* and Poisson's ratio; (**c**) relationship between Lame coefficient and *Vp*/*Vs*; (**d**) relationship between bulk modulus and Lame coefficient; (**e**) relationship between Poisson's ratio and Lame coefficient; (**f**) relationship between Lame coefficient and shear modulus. F-AP denotes fractures and dissolution pores samples. AP denotes dissolution pores samples.

The petrophysical response to fluids was analyzed using intersection plates. As is shown in Figure 5, the P-wave (*Vp*) and S-wave (*Vs*) velocities have no obvious distinction for water and gas saturation, and the P-wave impedance (*Ip*) and S-wave impedance (*Is*) also have a poor classification ability. The plot of the Poisson's ratio (σ) versus the P-wave velocity can better distinguish between samples containing water and gas [34–38]. This plot was divided into two areas (light yellow and light gray), and three samples were incorrectly classified (Figure 7b). The plots of the Lame coefficient versus *Vp*/*Vs* (Figure 7c), the bulk modulus (*K*) versus the Lame coefficient (Figure 7d), and the Poisson's ratio versus the Lame coefficient (Figure 7e) are also good for distinguishing between samples containing water and gas. In addition, three samples were incorrectly classified in Figure 7 c–e. The plot of the shear modulus (μ) versus Lame coefficient (λ) can also be used to distinguish between samples containing water and gas. Bounded by the auxiliary line, two samples were incorrectly classified (Figure 7f). Therefore, these two parameters can be used to further distinguish between samples containing gas and water. In conclusion, the results of this weathered granite reservoir provide a petrophysical basis for identifying gas- and water-containing formations.

5.3. Sensitivity of Different Physical Parameters for Gas in the Reservoir Space

In this study, the characteristics sensitive to the presence of gas were mainly investigated based on the parameters' variation characteristics for samples containing water and gas, and the gas-sensitive parameters were identified. The gas sensitivity index was calculated using the following formula [21,38]:

$$FS = (Aw - Ag)/Aw \tag{1}$$

where Aw is the petrophysical parameter value for a water-containing sample, and Ag is the petrophysical parameter value for a sample containing gas. FS is generally between -1 and 1, and the greater the absolute value of FS, the more sensitive parameter A is to the presence of gas in the reservoir space.

The shear parameters (e.g., Vs, Is, and μ) and bulk parameters (e.g., Ip, Vp, K, and λ) were calculated. The shear parameters and bulk parameters were constructed as combined parameters (e.g., $Ip^2 - 2.03\ Is^2$, K/μ, $\lambda - 0.03\ \mu$, $E - 2.03\ \mu$, and λ/μ). According to the combined parameters, the sensitivity indexes of the physical parameters were calculated. The arithmetic mean values of the shear parameters, bulk parameters, and combined parameters were compared, and in descending order to the sensitivities of the parameters are $Ip^2 - 2.03\ Is^2$, $\lambda - 0.03\ \mu$, λ, λ/μ, $E - 2.03\ \mu$, σ, K/μ, K, Ip, Vp/Vs, Vp, E, μ, Vs, and Is (Figure 8).

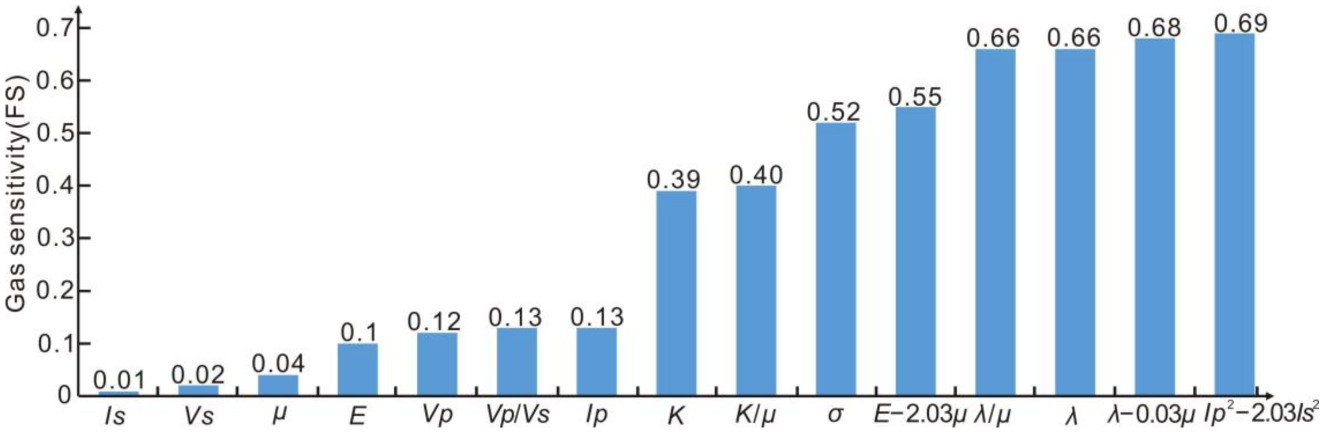

Figure 8. Sensitivity of different physical parameters for gas of Mesozoic granites in the coastal area of Fujian Province. *Ip*-P-wave impedance. *Is*-S-wave impedance. *Vp*-P-wave velocity. *Vs*-S-wave velocity. λ-Lame coefficient, two elastic constants in the relation between stress and strain of isotropic material under triaxiality stress state. μ-shear modulus, ratio of shear stress to strain. σ-Poisson's ratio, the ratio of the lateral strain to the axial strain in a uniaxial stress state. *E*-Young's modulus, the ratio of the extensional stress to the extensional strain in a uniaxial stress state. *K*-bulk modulus, the ratio of the hydrostatic stress to the volumetric strain. The parameter definition is quoted from Mavko et al. (2009) [38].

The results show that the shear parameters are not significantly sensitive to the presence of a fluid. The bulk parameters are significantly sensitive to the presence of a fluid, and most of the specific combination parameters are more responsive to the presence of a fluid. The combined parameters that include the Lame coefficient can more accurately distinguish between water and gas-containing samples. Furthermore, the gas-sensitive parameters for the identification of weathered granite reservoirs are λ and its combination parameters ($\lambda - 0.03\,\mu$ and λ/μ).

6. Discussion

6.1. Response of Reservoir Space Assemblage to Petrophysical Parameters

According to the assemblage of their reservoir spaces, the samples were divided into two types: samples containing fracture–dissolution pores and samples containing only dissolution pores. Based on the statistical analysis of the relevant parameters, the pore-type samples have a certain influence on the P-wave velocity (Table 3, Figure 9).

Table 3. The relevant parameters of Mesozoic granite reservoir space.

Reservoir Space	Porosity (%)	Dry Density (g/cm^3)	Water Saturated Density (g/cm^3)	Gas Saturated P-Wave Velocity (m/s)	Water Saturated P-Wave Velocity (m/s)	Note
Fracture dissolution pore	2.68~6.65	2.212~2.579	2.248~2.614	3500~5000	3500~5500	Primary value range
	4.70	2.474	2.554	3959	4540	Geometric mean
Dissolution pore	0.99~10.00	2.357~2.696	2.54~2.757	3500~6000	3500~6000	Primary value range
	3.35	2.554	2.597	4228	4758	Geometric mean

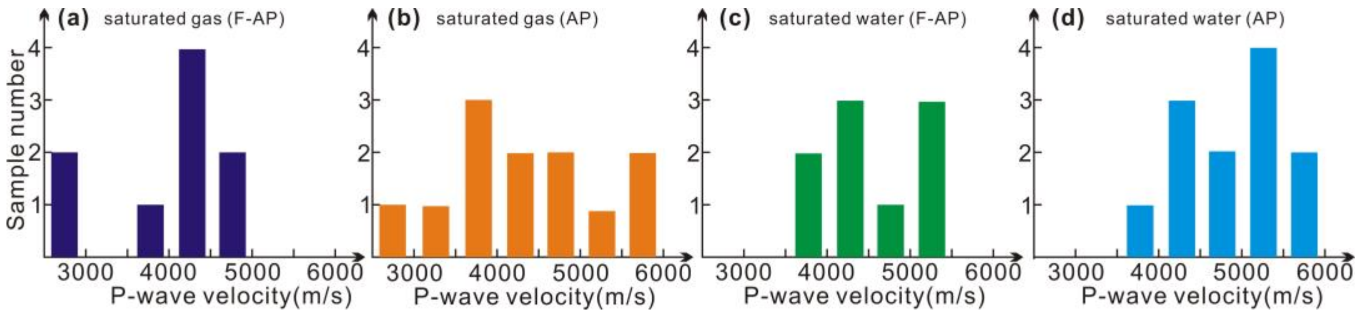

Figure 9. Response of the composition of the Mesozoic granite reservoir space to P-wave velocity. (**a**) P-wave velocity of gas-saturated fracture-dissolution pore samples; (**b**) P-wave velocity of gas-saturated dissolution pore samples; (**c**) P-wave velocity of water-saturated fracture-dissolution pore samples; (**d**) P-wave velocity of water-saturated dissolution pore samples. F-AP denotes fractures and dissolution pores samples. AP denotes dissolution pores samples.

The geometric mean porosity, density, and P-wave velocity values of the samples with these two types of reservoir spaces were compared. For weathered granite reservoirs, fractures can significantly reduce the density and P-wave velocity. Generally, fractures can reduce wave velocity due to their complementary nature (low pore stiffness and aspect ratio) [39–42]. The original granite pluton had a dense, massive structure without fractures and pores. Granite develops joints and fractures when undergoing tectonic stress. When the granite experienced uplift and erosion, platy joints and vertical joints formed due to the release of the loading stress. When the granite was exposed at the surface, physical weathering occurred and weathering fractures formed. Joints, fractures, and weathering fractures are all favorable channels for fluid migration. Dissolution pores often first develop at the locations of fracture planes [43]. Therefore, fractures control the development of dissolution pores. The dissolution pores are abundant near the fractures but are sparse far from the fractures. If fractures are developed in the sample, it suggests that the sample was taken from a reservoir area that is better for the storage of fluid. Biotite chloriteization, feldspar kaolinization, illiteization, and montmorillonization increase the porosity (Figure 2), which reduces the rock skeleton's density and the P-wave velocity. Field phenomena indicate that large fractures that are open fully or partially may further decrease P-wave velocity (Figure 2). In conclusion, the existence of fractures leads to a greater increase in porosity and decreases in the density and P-wave velocity.

6.2. Response of Reservoir Space Assemblage to Sensitivity of Petrophysical Parameters for Gas

The elastic parameters of the reservoir rock are affected by the properties of the skeleton medium, skeleton structure, and pore fluid [38,44]. The shear parameters are more responsive to the rock but not to the fluid, while the bulk parameters are responsive to the fluid [20,21]. The combined parameters constructed from different elastic parameters have a high fluid sensitivity. In this study, the sensitivities of the parameters to the presence of gas and water were discussed. Table 4 shows the sensitivities of the petrophysical parameters to the presence of gas are similar to the characteristic described above. In addition, the assemblage of the reservoir spaces exhibits a response to the gas sensitivity of the petrophysical parameters. The bulk modulus and K/μ are more sensitive than the bulk parameters and combination parameters, and their sensitivities are higher for the fracture-dissolution pore samples. The Lame coefficient, Poisson's ratio, λ/μ, $E - 2.03\ \mu$, $\lambda - 0.15\ \mu$, and$Ip^2 - 2.03\ Is^2$ parameters are more sensitive for the dissolution pore samples.

Table 4. Gas sensitivity of Mesozoic granite pore types to petrophysical parameters in the coastal area of Fujian Province.

Parameter	Sample Sensitivity		Parameter	Sample Sensitivity		Parameter	Sample Sensitivity	
	Fractures + Dissolution Pores	**Dissolution Pores**		**Fractures + Dissolution Pores**	**Dissolution Pores**		**Fractures + Dissolution Pores**	**Dissolution Pores**
Vp	0.14	0.10	K (bulk modulus)	0.42	0.36	$E - 2.03\mu$	0.46	0.61
Vs	−0.01	−0.02	E (Young's modulus)	0.09	0.08	$\lambda - 0.03\mu$	0.72	0.86
Vp/Vs	0.15	0.12	σ (Poisson's ratio)	0.44	0.58	$Ip^2 - 2.03Is^2$	0.73	0.86
K/μ	0.43	0.38	λ (Lame coefficient)	0.63	0.68	Ip (P-wave impedance)	0.15	0.11
λ/μ	0.63	0.69	μ (Shear modulus)	−0.01	−0.02	Is (S-wave impedance)	0.01	0.00

Note: the data in the table are the arithmetic means of 21 samples.

The bulk parameters mainly reflect the skeleton medium, structure, and the coupling between the skeleton and fluid. The X-ray diffraction results reveal that the samples contain a certain amount of clay minerals. Because hydration of the clay can cause the clay minerals volume to increase by up to 10 times, new skeletons are formed. Therefore, the pore volume will be reduced, and the P-wave propagation path will change when the sample contains water and gas [45–49]. In addition, the changes in the P-wave velocity and porosity become more obvious when the rock contains water and gas, and the sensitivity of the bulk and combination parameters to fluids increases. The dissolution pores are mainly intergranular micropores in the clay minerals such as chlorite, illite, and montmorillonite. The fractures in the samples are usually poorly filled. Regarding clay hydration, the degree of the hydration effect of the dissolution pore samples is stronger than that of the fracture–dissolution pore samples. Therefore, the bulk parameters and combination parameters of the dissolution pore samples are more sensitive to the presence of gas.

7. Conclusions

(1) The Cretaceous granite is predominantly monzogranite, and reservoir spaces are divided into fracture–dissolution pores and dissolution pores, characterized by medium-high densities and low-extra low porosities. The water and gas-containing samples can be effectively distinguished using parameters such as the Vp/Vs ratio, Poisson's ratio, and Lame coefficient.

(2) Through the analysis of the physical parameters of the Cretaceous granite, the shear parameters (Vs, Is, μ) are not sensitive to the presence of gas in the reservoir space. The bulk parameters (Ip, Vp, K, λ) are sensitive to the presence of gas. The combined parameters ($Ip^2 - 2.03\ Is^2$, K/μ, $\lambda - 0.03\ \mu$, $E - 2.03\ \mu$, λ/μ) are more sensitive to the presence of gas. From high to low, the sensitivities of the parameters are$Ip^2 - 2.03\ Is^2$, $\lambda - 0.03\ \mu$, λ, λ/μ, $E - 2.03\ \mu$, σ, K/μ, K, Ip, Vp/Vs, Vp, E, μ, Vs, and Is.

(3) For granite buried hill reservoir, the value ranges of density, P-wave velocity, and porosity of the fracture–dissolution pore granite samples are larger than those of the dissolution pore samples. The bulk parameters and combination parameters of the dissolution pore samples are more sensitive to gas capacity.

Author Contributions: Writing—original draft preparation, Z.T.; writing—review, J.L.; conceptualization and funding acquisition, H.T.; methodology, W.M. and Z.D.; investigation, resources, and data Curation, P.T. and J.H. All authors have read and agreed to the published version of the manuscript.

Funding: This study was supported by the Key R&D projects in Jilin Province (grant No.20230203107SF), the National Key R&D Program of China (grant No.2019YFC0605402) and the National Natural Science Foundation of China (grant No.41790453).

Data Availability Statement: Data see Appendix A.

Acknowledgments: We thank Quanbo Wen and Ningyuan Sun for the field work. Thanks to the three anonymous reviewers took the time to read this article and put forward their valuable comments.

Conflicts of Interest: The authors declare no conflict of interest.

Appendix A

The sample P-wave and S-wave velocities are obtained by Agilent MS07034B oscilloscope, Olympus 5077PR ultrasonic pulse generator and Olympus 1 MHz acoustic probe. The dynamic elastic parameters of rock are calculated by the velocity and time difference of P- and S-wave. The dynamic parameters of rock are mainly elastic Young's modulus (E), bulk modulus (K), shear modulus (μ), Poisson's ratio (σ), Lame coefficient (λ), P-wave impedance (Ip), and S-wave impedance (Is). The calculation formula is as follows.

Table A1. Sample parameters in gas saturated state.

Sample Number		Porosity (%)	Density (g/cm^3)	P-Wave Velocity (Vp) (m/s)	S-Wave Velocity (Vs) (m/s)	Vp/Vs	K/μ	λ/μ	Bulk Modulus (K)	Young's Modulus (E)	Poisson's Ratio (σ)	Lame Coefficient (λ) (GPa)	Shear Modulus (μ) (GPa)	$E-2.03\mu$	$\lambda-0.03\mu$	$Ip^2-2.03Is^2$	P-Wave Impedance (Ip)	S-Wave Impedance (Is)
Gas saturated state	JZ-2	10.00	2.36	3782.81	2500.50	1.51	0.96	0.29	14.08	32.77	0.11	4.25	14.74	2.86	3.81	8.98	8.92	5.89
	GW-CSC-9	2.68	2.57	4708.71	3095.56	1.52	0.98	0.31	24.15	55.14	0.12	7.73	24.63	5.14	6.99	17.96	12.10	7.96
	GW-CSC-10	7.52	2.46	3251.92	1820.47	1.79	1.86	1.19	15.17	20.77	0.27	9.72	8.17	4.19	9.48	23.35	8.01	4.49
	XP-MF-1	1.01	2.67	5506.66	3534.02	1.56	1.09	0.43	36.55	76.78	0.15	14.29	33.39	9.00	13.29	35.52	14.72	9.45
	XP-MF-6	3.41	2.60	3854.57	2325.41	1.66	1.41	0.75	19.85	34.07	0.21	10.49	14.04	5.58	10.07	26.14	10.00	6.04
	XP-MF-9	5.40	2.56	2840.60	1646.41	1.73	1.64	0.98	11.40	17.30	0.25	6.78	6.94	3.22	6.57	16.81	7.27	4.21
	XP-MF-10	3.61	2.21	4126.54	2561.96	1.61	1.26	0.59	18.30	34.44	0.19	8.63	14.52	4.98	8.19	18.12	9.13	5.67
	XP-MF-11	2.44	2.57	4359.82	3038.46	1.43	0.73	0.06	17.22	48.78	0.03	1.40	23.73	0.61	0.69	1.76	11.21	7.81
	XP-MF-14	6.65	2.52	4386.54	2794.12	1.57	1.13	0.46	22.22	45.51	0.16	9.13	19.64	5.64	8.54	21.47	11.04	7.03
	XP-MF-18	3.46	2.58	4751.04	2986.96	1.59	1.20	0.53	27.54	54.00	0.17	12.20	23.01	7.28	11.51	29.68	12.25	7.70
	XP-HWJ-1	0.99	2.55	5463.21	3622.87	1.51	0.94	0.27	31.47	74.10	0.11	9.17	33.45	6.19	8.16	20.80	13.92	9.23
	XP-SS-1	6.94	2.47	4284.84	2935.51	1.46	0.80	0.13	16.95	44.97	0.06	2.78	21.26	1.82	2.14	5.28	10.57	7.24
	XP-SS-2	6.12	2.70	3605.32	2487.03	1.45	0.77	0.10	12.81	34.89	0.05	1.69	16.68	1.04	1.19	3.21	9.72	6.71
	XP-BQ-3	6.56	2.43	4335.91	2843.06	1.53	0.99	0.33	19.52	44.17	0.12	6.41	19.67	4.24	5.82	14.16	10.55	6.92
	FD-LA-1	2.09	2.63	5013.05	3353.71	1.49	0.90	0.23	26.66	64.80	0.09	6.94	29.59	4.73	6.05	15.91	13.19	8.82
	FD-LA-3	3.37	2.65	4881.78	3305.77	1.48	0.85	0.18	24.52	62.31	0.08	5.23	28.94	3.56	4.36	11.55	12.93	8.75
	FD-NLG-4	5.52	2.47	4377.97	2923.27	1.50	0.91	0.24	19.17	46.26	0.10	5.12	21.07	3.49	4.49	11.06	10.79	7.21
	FD-NLG-6	5.23	2.48	2973.57	2006.16	1.48	0.86	0.20	8.64	21.64	0.08	1.97	10.00	1.35	1.67	4.15	7.39	4.98
	FD-TMS-4	2.83	2.52	2929.01	2007.09	1.46	0.80	0.13	8.07	21.43	0.06	1.31	10.13	0.86	1.01	2.54	7.37	5.05
	FD-TMS-6	4.90	2.48	3681.04	2488.71	1.48	0.85	0.19	13.10	33.09	0.08	2.88	15.33	1.96	2.42	5.99	9.11	6.16
	XP-DJHT-2	3.73	2.50	4738.53	3310.99	1.43	0.71	0.05	19.62	56.14	0.02	1.32	27.44	0.44	0.50	1.25	11.86	8.29

Table A2. Sample parameters in water saturated state.

Sample Number		Density (g/cm^3)	P-Wave Velocity (Vp) (m/s)	S-Wave Velocity (Vs) (m/s)	Vp/Vs	K/μ	λ/μ	Bulk Modulus (K)	Young's Modulus (E)	Poisson's Ratio (σ)	Lame Coefficient (λ) (GPa)	Shear Modulus (μ) (GPa)	$E-2.03\mu$	$\lambda-0.03\mu$	$Ip^2-2.03Is^2$	P-Wave Impedance (Ip)	S-Wave Impedance (Is)
Water saturated state	JZ-2	2.46	3634.16	2339.09	1.55	1.08	0.41	14.52	30.82	0.15	5.56	13.44	3.53	5.16	12.68	8.93	5.75
	GW-CSC-9	2.60	5172.95	3069.69	1.69	1.51	0.84	36.86	60.11	0.23	20.55	24.47	10.44	19.82	51.46	13.43	7.97
	GW-CSC-10	2.54	4041.67	1820.47	2.22	3.60	2.93	30.25	23.10	0.37	24.64	8.41	6.02	24.39	61.93	10.26	4.62
	XP-MF-1	2.68	5890.03	3534.02	1.67	1.44	0.78	48.41	81.69	0.22	26.07	33.51	13.66	25.06	67.24	15.80	9.48
	XP-MF-6	2.63	4969.69	2325.41	2.14	3.23	2.57	45.99	38.67	0.36	36.51	14.22	9.81	36.08	94.87	13.07	6.11
	XP-MF-9	2.61	3829.45	1646.41	2.33	4.08	3.41	28.88	19.64	0.39	24.16	7.08	5.26	23.94	62.57	10.01	4.30
	XP-MF-10	2.25	5074.65	2561.96	1.98	2.59	1.92	38.21	39.21	0.33	28.38	14.75	9.26	27.93	62.78	11.41	5.76
	XP-MF-11	2.59	5116.58	3038.46	1.68	1.50	0.84	35.99	58.82	0.23	20.02	23.96	10.19	19.30	50.09	13.28	7.88
	XP-MF-14	2.58	4947.92	2794.12	1.77	1.80	1.14	36.34	51.04	0.27	22.90	20.16	10.12	22.29	57.56	12.78	7.21
	XP-MF-18	2.61	5252.29	2986.96	1.76	1.76	1.09	41.01	58.81	0.26	25.47	23.32	11.47	24.77	64.73	13.73	7.81

Table A2. *Cont.*

Sample Number	Density (g/cm^3)	P-Wave Velocity (Vp) (m/s)	S-Wave Velocity (Vs) (m/s)	Vp/Vs	K/μ	λ/μ	Bulk Modulus (K)	Young's Modulus (E)	Poisson's Ratio (σ)	Lame Co-efficient (λ) (GPa)	Shear Modulus (μ) (GPa)	$E-2.03\mu$	$\lambda-0.03\mu$	$Ip^2-2.03Is^2$	P-Wave Impedance (Ip)	S-Wave Impedance (Is)
XP-HWJ-1	2.56	5690.21	3589.11	1.59	1.18	0.51	38.90	77.10	0.17	16.93	32.96	10.19	15.94	40.78	14.56	9.18
XP-SS-1	2.54	4516.75	2768.56	1.63	1.33	0.66	25.82	46.62	0.20	12.86	19.44	7.16	12.28	31.14	11.46	7.02
XP-SS-2	2.76	4235.21	2487.03	1.70	1.57	0.90	26.72	42.19	0.24	15.35	17.06	7.57	14.84	40.91	11.68	6.86
XP-BQ-3	2.50	4408.63	2843.06	1.55	1.07	0.40	21.63	46.21	0.14	8.17	20.20	5.21	7.56	18.90	11.02	7.10
FD-LA-1	2.65	5158.06	3222.12	1.60	1.23	0.56	33.84	64.98	0.18	15.49	27.53	9.09	14.66	38.89	13.68	8.54
FD-LA-3	2.68	5082.73	3186.99	1.59	1.21	0.54	32.96	64.07	0.18	14.80	27.24	8.77	13.99	37.51	13.63	8.55
FD-NLG-4	2.52	4488.80	2710.17	1.66	1.41	0.74	26.11	44.93	0.21	13.76	18.52	7.34	13.21	33.29	11.32	6.83
FD-NLG-6	2.54	3791.57	2006.16	1.89	2.24	1.57	22.85	26.66	0.31	16.05	10.21	5.93	15.74	39.93	9.62	5.09
FD-TMS-4	2.54	4042.83	2007.09	2.01	2.72	2.06	27.92	27.39	0.34	21.08	10.25	6.59	20.78	52.86	10.29	5.11
FD-TMS-6	2.52	4178.48	2390.18	1.75	1.72	1.06	24.85	36.25	0.26	15.23	14.42	6.98	14.80	37.36	10.55	6.03
XP-DJHT-2	2.54	5312.66	3310.99	1.60	1.24	0.57	34.57	65.86	0.18	16.00	27.85	9.33	15.17	38.53	13.50	8.41

Table A3. Sample sensitive parameters.

	Sample Number	P-Wave Velocity (Vp) (m/s)	S-Wave Velocity (Vs) (m/s)	Vp/Vs	K/μ	λ/μ	Bulk Modulus (K)	Young's Modulus (E)	Poisson's Ratio (σ)	Lame Co-efficient (λ) (GPa)	Shear Modulus (μ) (GPa)	$E-2.03\mu$	$\lambda-0.03\mu$	$Ip^2-2.03Is^2$	P-Wave Impedance (Ip)	S-Wave Impedance (Is)
Sensitive parameter (FS)	JZ-2	−0.04	−0.07	0.03	0.12	0.30	0.03	−0.06	0.23	0.24	−0.10	0.19	0.24	0.00	0.00	−0.03
	GW-CSC-9	0.09	−0.01	0.10	0.35	0.63	0.34	0.08	0.48	0.62	−0.01	0.51	0.62	0.01	0.10	0.00
	GW-CSC-10	0.20	0.00	0.20	0.48	0.59	0.50	0.10	0.27	0.61	0.03	0.30	0.60	0.05	0.22	0.03
	XP-MF-1	0.07	0.00	0.07	0.24	0.45	0.25	0.06	0.31	0.45	0.00	0.34	0.45	0.00	0.07	0.00
	XP-MF-6	0.22	0.00	0.22	0.56	0.71	0.57	0.12	0.41	0.71	0.01	0.43	0.71	0.05	0.23	0.01
	XP-MF-9	0.26	0.00	0.26	0.60	0.71	0.61	0.12	0.36	0.72	0.02	0.39	0.72	0.07	0.27	0.02
	XP-MF-10	0.19	0.00	0.19	0.51	0.69	0.52	0.12	0.43	0.70	0.02	0.46	0.70	0.04	0.20	0.02
	XP-MF-11	0.15	0.00	0.15	0.52	0.93	0.52	0.17	0.88	0.93	0.01	0.94	0.93	0.02	0.16	0.01
	XP-MF-14	0.11	0.00	0.11	0.37	0.59	0.39	0.11	0.40	0.60	0.03	0.44	0.60	0.02	0.14	0.03
	XP-MF-18	0.10	0.00	0.10	0.32	0.51	0.33	0.08	0.34	0.52	0.01	0.37	0.52	0.01	0.11	0.01
	XP-HWJ-1	0.04	−0.01	0.05	0.20	0.47	0.19	0.04	0.37	0.46	−0.01	0.39	0.46	0.00	0.04	−0.01
	XP-SS-1	0.05	−0.06	0.11	0.40	0.80	0.34	0.04	0.71	0.78	−0.09	0.75	0.79	0.00	0.08	−0.03
	XP-SS-2	0.15	0.00	0.15	0.51	0.89	0.52	0.17	0.81	0.89	0.02	0.86	0.89	0.03	0.17	0.02
	XP-BQ-3	0.02	0.00	0.02	0.07	0.19	0.10	0.04	0.15	0.22	0.03	0.19	0.21	0.00	0.04	0.03
	FD-LA-1	0.03	−0.04	0.07	0.27	0.58	0.21	0.00	0.47	0.55	−0.07	0.48	0.55	0.00	0.04	−0.03
	FD-LA-3	0.04	−0.04	0.07	0.30	0.67	0.26	0.03	0.57	0.65	−0.06	0.59	0.65	0.00	0.05	−0.02
	FD-NLG-4	0.02	−0.08	0.10	0.35	0.67	0.27	−0.03	0.54	0.63	−0.14	0.53	0.63	0.00	0.05	−0.05
	FD-NLG-6	0.22	0.00	0.22	0.61	0.87	0.62	0.19	0.73	0.88	0.02	0.77	0.88	0.05	0.23	0.02
	FD-TMS-4	0.28	0.00	0.28	0.71	0.94	0.71	0.22	0.83	0.94	0.01	0.87	0.94	0.08	0.28	0.01
	FD-TMS-6	0.12	−0.04	0.15	0.50	0.82	0.47	0.09	0.69	0.81	−0.06	0.72	0.81	0.02	0.14	−0.02
	XP-DJHT-2	0.11	0.00	0.11	0.42	0.92	0.43	0.15	0.87	0.92	0.01	0.95	0.92	0.01	0.12	0.01

Table A4. The dynamic parameters calculation formula.

Parameter	Young's Modulus(E)	Bulk Modulus (K)		Shear Modulus (μ)
formula	$E = \frac{\rho_b \times 10^9 \times \left(3 \times \Delta t_s^2 - 4 \times \Delta t_p^2\right)}{\Delta t_s^2 \times \left(\Delta t_s^2 - \Delta t_p^2\right)}$	$K = \frac{\rho_b \times 10^9 \times \left(3 \times \Delta t_s^2 - 4 \times \Delta t_p^2\right)}{3 \times \Delta t_s^2 \times \Delta t_p^2}$		$\mu = \frac{\rho_b \times 10^9}{\Delta t_s^2}$
parameter	Poisson's ratio (σ)	Lame coefficient (λ)	P-wave impedance (Ip)	S-wave impedance (Is)
formula	$\sigma = \frac{\Delta t_s^2 - 2 \times \Delta t_p^2}{2 \times \left(\Delta t_s^2 - \Delta t_p^2\right)}$	$\lambda = \frac{3 \times K \times \mu}{1 + \mu}$	$Ip = \rho_b \times V_p$	$Is = \rho_b \times V_S$

Note: ρ_b, Δt_s, Δt_p, V_P and vs. are rock density (g/cm^3), S-wave time difference (us/m), P-wave time difference (us/m), P-wave velocity (m/s), and S-wave velocity (m/s), respectively. The relevant formulas and details can be found in Mavko et al. (2009) [38].

References

1. Pan, C.H. Petroleum in basement rocks. *AAPG Bull.* **1982**, *66*, 1597–1643.
2. Li, J.; Liu, L.F.; Zhao, Y.H.; Tu, G.H.; Zhou, L.H.; Xiao, D.Q.; Gao, J.D. A review of study on ancient buried hill reservoir. *Prog. Geophys.* **2006**, *21*, 879–887.
3. Yang, F.; Xu, S.Y. Global distribution and hydrocarbon accumulation pattern of basement reservoirs. *Spec. Oil Gas Reserv.* **2011**, *18*, 7–11.
4. Cuong, T.X.; Warren, J.K. Bach ho field, a fractured granitic basement reservoir, Cuu Long basin offshore SE Vietnam: A "buried-hill" play. *J. Pet. Geol.* **2009**, *32*, 129–156. [CrossRef]
5. Deng, Y.H. Formation mechanism and exploration practice of large-medium buried-hill oil fields in Bohai Sea. *Acta Petrolei Sin.* **2015**, *36*, 253–261. [CrossRef]
6. Dou, L.R.; Wei, X.D.; Wang, J.C.; Li, J.L.; Wang, R.C.; Zhang, S.H. Characteristics of granitic basement rock buried-hill reservoir in Bongor Basin, Chad. *Acta Petrolei Sin.* **2015**, *36*, 897–904+925. [CrossRef]
7. Xie, Y.H. Practices and thoughts of CNOOC offshore oil and gas exploration. *China Offshore Oil Gas* **2020**, *32*, 1–13. [CrossRef]
8. Li, W.; Liu, Y.K.; Chen, Y.; Liu, B.J.; Feng, S.Y. Active source seismic imaging on near-surface granite body: Case study of siting a geological disposal repository for high-level radioactive nuclear waste. *Pet. Sci.* **2021**, *18*, 742–757. [CrossRef]
9. Zhou, X.H.; Wang, Q.B.; Feng, C. Formation conditions and geological significance of large Archean buried hill reservoirs in Bohai Sea. *Earth Sci.* **2021**, *36*, 253–261. [CrossRef]
10. Wang, X.; Zhou, X.H.; Xu, G.S.; Liu, P.B.; Gao, K.S.; Guan, D.Y. Characteristics and controlling factors of reservoirs in Penglai 9-1 large-scale oilfield in buried granite hills, Bohai Sea. *Oil Gas Geol.* **2015**, *36*, 262–270. [CrossRef]
11. Chen, G.Q.; Chen, H.J.; Tian, X.P. Characteristics and controlling factors of granitic buried-hill reservoir in PL oilfield of Bohai Sea. Mar. *Geol. Front.* **2016**, *32*, 14–19+65. [CrossRef]
12. Xu, S.L.; You, L.; Mao, X.L.; Zhong, J.; Wu, S.J. Reservoir Characteristics and Controlling Factors of Granite Buried Hill in Songnan Low Uplift, Qiongdongnan Basin. *Earth Sci.* **2019**, *44*, 2717–2728. [CrossRef]
13. Xue, Y.A.; Wang, Q.; Niu, C.M. Hydrocarbon charging and accumulation of BZ 19-6 gas condensate field in deep buried hills of Bozhong Depression, Bohai Sea. *Oil Gas Geol.* **2020**, *41*, 891–902. [CrossRef]
14. Hu, Z.W.; Xu, C.G.; Yang, B.; Huang, Z.; Su, W. Reservoir forming mechanism of Penglai 9-1 granite buried-hills and its oil geology significance in Bohai Sea. *Acta Petrolei Sin.* **2017**, *38*, 274–285. [CrossRef]
15. Luo, W.; Cai, J.J.; Wan, Q.H.; Gao, X.; Yan, P. Reservoir condition analysis of a buried granite hill in the Huizhou Depression and its petroleum geological significance. *Mar. Geol. Quat. Geol.* **2019**, *39*, 126–135. [CrossRef]
16. Holdsworth, R.E.; Trice, R.; Hardman, K.; McCaffrey, K.J.W.; Morton, A.; Frei, D.; Dempsey, E.; Bird, A.; Rogers, S. The nature and age of basement host rocks and fissure fills in the Lancaster field fractured reservoir, West of Shetland. *J. Geol. Soc.* **2020**, *177*, 1057–1073. [CrossRef]
17. McCaffrey, K.J.W.; Holdsworth, R.E.; Pless, J.; Franklin, B.S.G.; Hardman, K. Basement reservoir plumbing: Fracture aperture, length and topology analysis of the Lewisian Complex, NW Scotland. *J. Geol. Soc.* **2020**, *177*, 1281–1293. [CrossRef]
18. Ye, T.; Niu, C.M.; Wei, A.J. Characteristics and genetic mechanism of large granitic buried-hill reservoir, a case study from PengLai oil field of Bohai Bay Basin, north China. *J. Pet. Sci. Eng.* **2020**, *189*, 106988. [CrossRef]
19. Chen, X.L.; Zhao, Z.P.; Hui, G.Z.; Zhao, J. Characteristics of weathered metamorphic rocks crust in Bohai Sea and its quantitative prediction. *Mar. Geol. Front.* **2021**, *37*, 33–41. [CrossRef]
20. Sun, X.G.; Wei, W.; Li, H.M. Fluid sensitivity analysis of petrophysical parameters. *Reserv. Eval. Dev.* **2012**, *2*, 37–49. [CrossRef]
21. Chen, S.M.; Li, L.L.; Zhao, H.B. Physical analysis of acoustic characteristics of Cretaceous volcanic rocks in the Songliao basin. *Acta Petrol. Sin.* **2010**, *26*, 14–20.
22. Zhang, S.W.; Sun, J.M.; Su, J.L.; Gan, L. Experimental analysis for the physical and elastic parameters of Archean buried hill rock. *Well Logging Technol.* **2010**, *34*, 522–526.
23. Liu, J.S.; Xu, H.Z.; Jiang, Y.M.; Wang, J.; He, X.J. Mesozoic and Cenozoic basin structure and tectonic evolution in the East China Sea basin. *Acta Geol. Sin.* **2020**, *94*, 675–691. [CrossRef]

24. Nguyen, T.B.T.; Satir, M.; Siebel, W.; Vennemann, T.; Van Long, T. Geochemical and isotopic constraints on the petrogenesis of granitoids from the Dalat zone, southern Vietnam. *J. Asian Earth Sci.* **2004**, *23*, 467–482. [CrossRef]
25. Honza, E.; Fujioka, K. Formation of arcs and backarc basins inferred from the tectonic evolution of Southeast Asia since the Late Cretaceous. *Tectonophysics* **2004**, *384*, 23–53. [CrossRef]
26. Mao, J.R.; Li, Z.L.; Ye, H.M. Mesozoic tectono-magmatic activities in South China: Retrospect and prospect. *Sci. China Earth Sci.* **2014**, *57*, 2853–2877. [CrossRef]
27. Yan, Q.S.; Shi, X.F.; Castillo, P.R. The late Mesozoic-Cenozoic tectonic evolution of the South China Sea: A petrologic perspective. *J. Asian Earth Sci.* **2014**, *85*, 178–201. [CrossRef]
28. Yan, Q.S.; Metcalfe, I.; Shi, X.F. U-Pb isotope geochronology and geochemistry of granites from Hainan Island (northern South China Sea margin): Constraints on late Paleozoic-Mesozoic tectonic evolution. *Gondwana Res.* **2017**, *49*, 333–349. [CrossRef]
29. Hennig, J.; Breitfeld, H.T.; Hall, R.; Surya Nugraha, A.M. The Mesozoic tectono-magmatic evolution at the Paleo-Pacific subduction zone in West Borneo. *Gondwana Res.* **2017**, *48*, 292–310. [CrossRef]
30. Fu, X.W.; Zhu, W.L.; Chen, C.F.; Zhong, K.; Xu, C.H. Detrital zircon provenance of upper Mingyuefeng Formation in west slope of Lishui-Jiaojiang sag, the East China Sea. *Earth. Sci. J. Chin. Univ. Geosci.* **2015**, *40*, 1987–2001. [CrossRef]
31. Li, J.Z.; Liu, P.Y.; Zhang, J.L.; Sun, S.Y.; Sun, Z.F.; Du, D.X.; Zhang, M. Base level changes based on Basin Filling Modelling: A case study from the Paleocene Lishui Sag, East China Sea Basin. *Pet. Sci.* **2020**, *17*, 1195–1208. [CrossRef]
32. Xu, N.C.; Shen, J.L.; Zhang, J. Application of X-ray diffraction, X-ray fluorescence spectrometry and electron microprobe in the identification of basalt. *Rock Miner. Anal.* **2015**, *34*, 75–81. [CrossRef]
33. Li, G.M. The assessment of measuring the porosity of core using fluid saturation method. *Metrol. Meas. Tech.* **2012**, *39*, 83–84.
34. Batzle, M.; Wang, Z. Seismic properties of pore fluids. *Geophysics* **1992**, *57*, 1396–1408. [CrossRef]
35. Batzle, M.; Hofmann, R.; Han, D.-H.; Castagna, J.P. Fluids and frequency dependent seismic velocity of rocks. *Lead. Edge* **2001**, *2*, 168–171. [CrossRef]
36. Klimentos, T. Attenuation of P- and S-waves as a method of distinguishing gas and condensate from oil and water. *Geophysics* **1995**, *60*, 447–458. [CrossRef]
37. Chapman, M.; Liu, E.; Li, X.Y. The influence of fluid-sensitive dispersion and attenuation on AVO analysis. *Geophys. J. Int.* **2006**, *167*, 89–105. [CrossRef]
38. Mavko, G.; Mukerji, T.; Dvorkin, J. *The Rock Physics Handbook: Fluid Effects on Propagation*; Cambridge University Press: Cambridge, UK, 2009; pp. 266–346.
39. El-Husseiny, A.; Vega, S.; Nizamuddin, S. The effect of pore structure complexity and saturation history on the variations of acoustic velocity as function of brine and oil saturation in carbonates. *J. Pet. Sci. Eng.* **2019**, *179*, 180–191. [CrossRef]
40. Fournier, F.; Pellerin, M.; Villeneuve, Q.; Teillet, T.; Hong, F.; Poli, E.; Borgomano, J.; Léonide, P.; Hairabian, A. The equivalent pore aspect ratio as a tool for pore type prediction in carbonate reservoirs. *AAPG Bull.* **2018**, *102*, 1343–1377. [CrossRef]
41. Jaballah, J.; Reijmer, J.J.G.; El-Husseiny, A.; Le Goff, J.; Hairabian, A.; Slootman, A. Physical properties of Cretaceous to Eocene platform-to-basin carbonates from Albania. *Mar. Pet. Geol.* **2021**, *128*, 105022. [CrossRef]
42. Weger, R.J.; Eberli, G.P.; Baechle, G.T.; Massaferro, J.L.; Sun, Y.-F. Quantification of pore structure and its effect on sonic velocity and permeability in carbonates. *AAPG Bull.* **2009**, *93*, 1297–1317. [CrossRef]
43. Tang, H.F.; Tian, Z.W.; Gao, Y.F.; Dai, X.J. Review of volcanic reservoir geology in China. *Earth Sci. Rev.* **2022**, *232*, 104158. [CrossRef]
44. Li, W.X.; Shi, G.; Wang, H.; Yao, Z.X. The study on the relationships of elastic properties of rock physics. *Prog. Geophys.* **2007**, *22*, 1380–1385.
45. Sposito, G.; Prost, R. Structure of water adsorbed on smectites. *Chem. Rev.* **1982**, *82*, 553–573. [CrossRef]
46. Bird, P. Hydration phase diagrams and friction of montmorillonite under laboratory and geologic conditions, with implications for shale compaction, slope stability, and strength of fault gauge. *Tectonophysics* **1984**, *107*, 235–260. [CrossRef]
47. Suzuki, S.; Prayongphan, S.; Ichikawa, Y.; Chae, B. In situ observations of the swelling of bentonite aggregates in NACL solution. *Appl. Clay Sci.* **2005**, *29*, 89–98. [CrossRef]
48. Déekany, I.; Berger, F. Adsorption from liquid mixtures on solid surfaces. In *Adsorption Theory, Modeling, and Analysis*; Tóth, J., Ed.; Marcel Dekker, Inc.: New York, NY, USA, 2002; pp. 573–630.
49. Zhang, L.H.; Lu, X.C.; Liu, X.D.; Zhou, J.H.; Zhou, H.Q. Hydration and mobility of interlayer ions of (Na_x,Ca_y)-montmorillonite: A molecular dynamics study. *J. Phys. Chem. C* **2014**, *118*, 29811–29821. [CrossRef]